PHYSICAL REVIEW B **105**, 214428 (2022)

Tuning magnetic anisotropy and Dzyaloshinskii-Moriya interaction via interface engineering in nonisostructural $SrCuO_2/SrRuO_3$ heterostructures

Xiaobing Chen,[1,2,*] Jine Zhang,[3,*] Banggui Liu,[1,2] Fengxia Hu,[1,2,4] Baogen Shen,[1,2,4] and Jirong Sun[1,2,4,5,†]
[1]*Beijing National Laboratory for Condensed Matter Physics & Institute of Physics,*
Chinese Academy of Sciences, Beijing 100190, People's Republic of China
[2]*School of Physical Sciences, University of Chinese Academy of Sciences, Beijing 100049, People's Republic of China*
[3]*School of Integrated Circuit Science and Engineering, Beihang University, Beijing 100191, People's Republic of China*
[4]*Songshan Lake Materials Laboratory, Dongguan, Guangdong 523808, People's Republic of China*
[5]*Spintronics Institute, University of Jinan, Jinan, Shandong 250022, People's Republic of China*

(Received 2 November 2021; revised 30 May 2022; accepted 8 June 2022; published 23 June 2022)

We report a theoretical investigation on the effects of interface reconstruction on magnetic anisotropy (MA) and Dzyaloshinskii-Moriya interaction (DMI) for nonisostructural heterostructures formed by an infinite-layer oxide $SrCuO_2$ and a perovskite oxide $SrRuO_3$. Due to the atomic, charge, spin, and orbital reconstructions at interface, the SRO film thickness-dependent magnetic anisotropy oscillation behavior has been greatly tuned in two $SrCuO_2/SrRuO_3$ heterostructures. A strong DMI of 3.5 meV/Ru and a large DMI/exchange constant ratio $|D/J|$ of 0.63 are obtained at the CuO_2-Sr-RuO_2 interface, which are beneficial to the creation and stability of skyrmions. Besides, the DMI is tunable, monotonically decreasing with the increase of the content of the apical oxygen ions in the interfacial layer, and takes the minimal value of 0.1 meV/Ru at the CuO_2-SrO-RuO_2 interface. We evaluate the formation energy of oxygen vacancy in interface SRO layer, which turns out to be half as much as that in bulk SRO. This small value ensures the experimental feasibility towards two interfaces. Combining first-principles calculations with tight-binding model, we find that the effectively modulated MA and DMI at the CuO_2-Sr-RuO_2 interface are mainly associated with the occupation of $d_{3z^2-r^2}$ orbital, the enhanced interface symmetry breaking, and orbital hybridization. The present work demonstrates the distinct features of the interface formed between nonisostructural oxides and suggests a conceptually different strategy towards the modulation of MA and DMI.

DOI: 10.1103/PhysRevB.105.214428

I. INTRODUCTION

Spin manipulation is of major interest due to the novel physics involved and the emergence of spin orbitronics such as spin-momentum locking [1,2], spin Hall effect [3,4], and topological spin textures [5,6]. Among these phenomena, chiral magnetic skyrmions are especially attractive since they display high current-velocity characteristics [7,8]. Generally speaking, stable skyrmions are the result of the competition among the Dzyaloshinskii-Moriya interaction (DMI), magnetic anisotropy (MA), and the Heisenberg exchange interaction. Therefore, magnetic materials with strong and tunable DMI are highly desired, which may host tunable skyrmions that are required by practical application.

DMI can be effectively tuned via interface engineering, since it stems from the spin-orbit coupling (SOC) and the inversion symmetry breaking [9]. Meanwhile, different interfaces will result in a variety of MA. Perovskite oxides are promising candidates for interface engineering. Many different approaches have been attempted for tuning the MA and DMI at perovskite/perovskite interface [10–15]. For example, a giant topological Hall effect and a large perpendicular magnetic anisotropy have been observed in the $La_{0.7}Sr_{0.3}MnO_3$ films in proximity to $SrIrO_3$, an oxide with strong SOC [10,11]. Besides, the manipulation of MA and DMI can be achieved by tuning the degree of the inversion symmetry breaking, such as tuning oxygen octahedron rotation and tilting [12], controlling the interface termination [13], introducing the oxygen defect [14], and inserting a ferroelectric proximity layer [15]. However, it remains a challenge to realize a sizable DMI to meet the size of spin textures for practical applications in high density devices.

Recently, a nonisostructural interface was found to show strong interfacial reconstructions due to the mismatch of oxygen sublattice at the interface, resulting in physical properties not envisaged in bulk material [16–19]. Meanwhile, oxygen sublattice mismatch provides spare space for selective control of interfacial chemical bonding, for the modification of polyhedral connectivity at interface and for the artificial design of the degree of interfacial inversion symmetry breaking.

In this work, we present a systematic investigation of the nonisostructural $SrCuO_2/SrRuO_3$ (SCO/SRO) heterostructures with two different interfacial structures, CuO_2-Sr-RuO_2 and CuO_2-SrO-RuO_2. Different interfacial structures result in different interfacial bonding geometries as shown Figs. 1(a)

---

[*] These authors contributed equally to this work.
[†] Corresponding author: jrsun@iphy.ac.cn

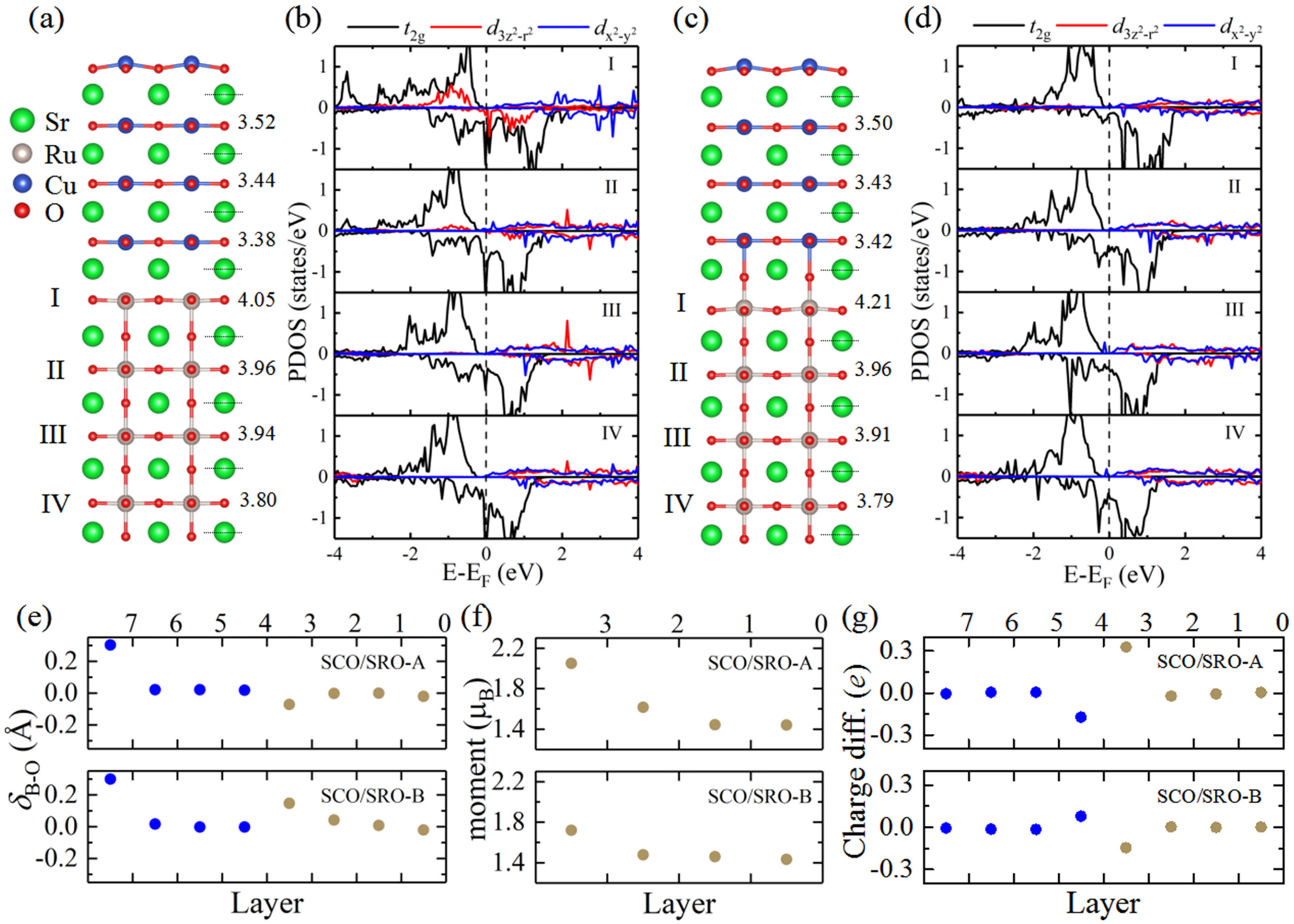

FIG. 1. Optimized lattice structures of SCO/SRO heterostructures with (a) CuO$_2$-Sr-RuO$_2$ and (c) CuO$_2$-SrO-RuO$_2$ interface for the $t_{\mathrm{SRO}} =$ 4 uc case. The Sr-Sr distance are also shown. (b),(d) Corresponding orbital-decomposed projected density of states (PDOS) of different SRO layers. The Fermi level is set to zero in energy and marked by dashed lines. (e) Layer-resolved vertical displacement $\delta_{B\text{-}O}$ of the B sites from their respective oxygen layers. Here B denotes Cu and Ru in SCO and SRO layers, respectively. (f) Layer-resolved projected magnetic moments of Ru ions. (g) Layer-resolved charge difference at Cu and Ru sites relative to those of corresponding atoms in bare SCO and SRO films. The layer indices 0–7 in (e)–(g) denote the Sr/SrO layer in heterostructures from bottom to top.

and 1(c). Based on first-principles calculations, we provide a quantitative description for atomic, charge, spin, and orbital reconstructions around interface. Besides, the formation energy of oxygen vacancy in interfacial SRO layer is reduced to half as much as that in bulk SRO, thus we expect that the CuO$_2$-Sr-RuO$_2$ interface is easy to fabricate experimentally. Meanwhile, by controlling the oxygen atmosphere, the CuO$_2$-SrO-RuO$_2$ interface can be obtained. We found an oscillation of magnetocrystalline anisotropy energy (MCA) with the layer thickness of SRO ((t_{SRO}). Besides, the MCA-t_{SRO} oscillation of two heterostructures are both different from that in corresponding bare SRO films. Moreover, a strong DMI strength of 3.5 meV/Ru at the CuO$_2$-Sr-RuO$_2$ interface is obtained. Remarkably, the DMI strength is tunable when changing the oxygen content of the interfacial Sr layer. It takes the minimal value of 0.1 meV/Ru when the interface layer becomes CuO$_2$-SrO-RuO$_2$. Further investigations demonstrate that the occupation of $d_{3z^2-r^2}$ orbital and the inversion symmetry breaking affect both MA and DMI.

II. METHODS

Density functional theory (DFT) calculations were performed within the projected augmented-wave method [20] as implemented in the Vienna *ab initio* simulation package codes [21,22]. The generalized gradient approximation of Perdew-Burke-Ernzerhof modified for solids was adopted for the calculation of exchange-correlation energy [23,24]. A cutoff energy of 600 eV was found to achieve numerical convergence. The Brillouin zone was sampled with 13 × 13 × 13 and 13 × 13 × 1 Monkhorst-Pack meshes [25] for bulk SRO and SCO/SRO heterostructures, respectively. The convergence criteria of total energy and atomic force were 10^{-5} eV and 0.01 eV Å^{-1} in collinear calculations. Gaussian smearing of the electron occupations was applied with a width of 0.05 eV. The effects of the smearing parameters on the oscillations of the MCA energy are also given in Fig. S4 of the Supplemental Material [26]. To consider the correlation effects of Ru 4d electrons, the on-site Coulomb interaction of $U_{\mathrm{eff}} = 2.1$ eV [27] was used within the rotationally invariant Dudarev's formalism [28]. The on-site Coulomb interaction of

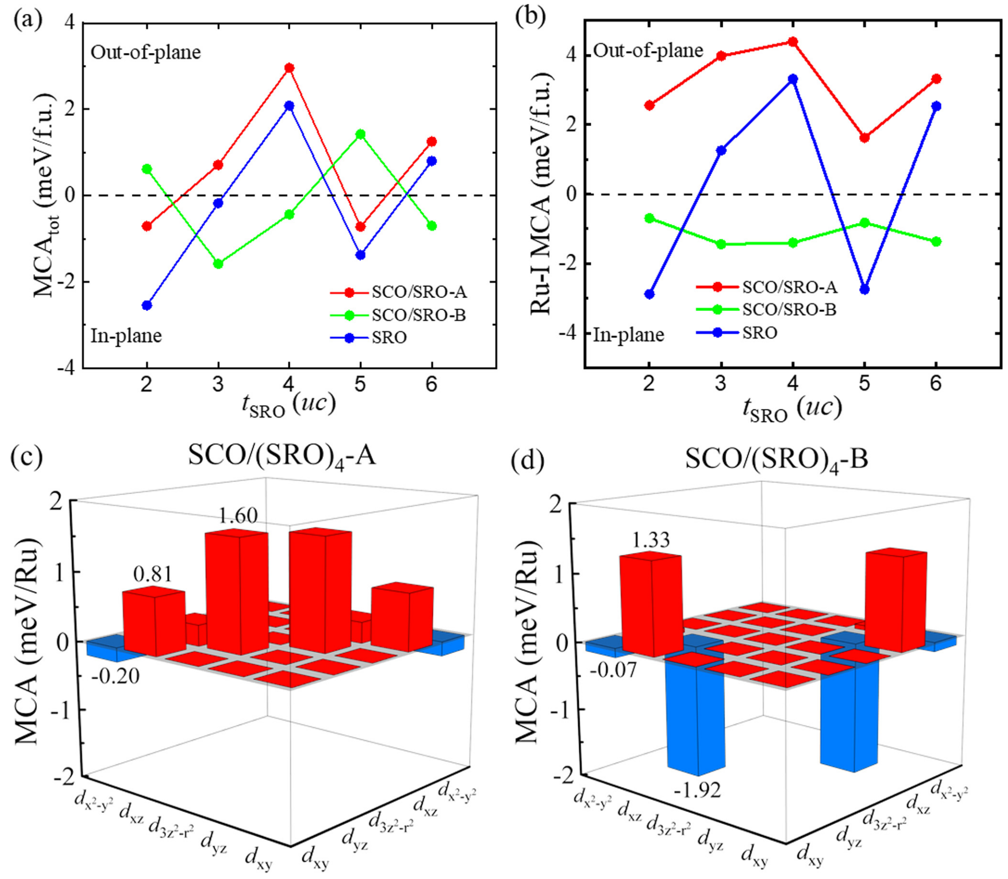

FIG. 2. (a) Total MCA and (b) the MCA of interfacial Ru ion as functions of t_{SRO}. Orbital-resolved MCA for the interfacial Ru ion in (c) SCO/SRO-*A* and (d) SCO/SRO-*B* heterostructures ($t_{\mathrm{SRO}} = 4$ uc). Orbital-resolved MCA for the interfacial Ru ion with different t_{SRO} show largely identical results as shown in Fig. S3 [26].

$U_{\mathrm{eff}} = 6.5$ eV [29] was used for the Cu 3*d* electrons. We also confirmed that a smaller value of $U_{\mathrm{eff}} = 4$ or 0 eV [30,31] for Cu 3*d* electrons leads to similar results.

To simulate the epitaxially grown SCO/SRO heterostructures, we constructed slab models as shown in Figs. 1(a) and 1(c), in which we stacked 4 unit cells (uc) on 2–6 uc SRO, with the $\mathrm{RuO_2}$- or SrO-terminated surface in contact with the SCO layer, respectively. In the *z* direction, the vacuum region spanned 15 Å to prohibit the interactions between neighboring heterostructures and the dipole correction was applied to remove artificial dipole interaction [32]. The in-plane lattice constant was fixed at the experimental value of the $\mathrm{SrTiO_3}$ substrate ($a = 3.905$ Å). We confirmed that main results are similar using the $\sqrt{2} \times \sqrt{2}$ supercells. The lattice distortion in SRO ($a_{\mathrm{pc}} = 3.93$ Å) was ignored in this work for simplicity as it can be effectively suppressed under compressive strain [33].

MCA can be calculated by force theorem and defined as the total energy difference between in-plane and out-of-plane magnetization orientation in the presence of SOC in VASP [34,35], i.e., $\mathrm{MCA_{tot}} = E^{\parallel}_{\mathrm{tot}} - E^{\perp}_{\mathrm{tot}}$. In detail, self-consistent calculations without SOC were performed first and then non-self-consistent calculations with SOC were performed with different magnetization orientations. The particular formulation of the total MCA can be expressed as follows [36–38]:

$$\mathrm{MCA_{tot}} = E^{\parallel}_{\mathrm{tot}} - E^{\perp}_{\mathrm{tot}} \approx \sum_{k}^{N_k} \sum_{n}^{N_b} \left[f^{\parallel}(\epsilon^{\parallel}_{kn})\epsilon^{\parallel}_{kn} - f^{\perp}(\epsilon^{\perp}_{kn})\epsilon^{\perp}_{kn} \right], \tag{1}$$

where $E^{\parallel,\perp}_{\mathrm{tot}}$ are the total energy in non-self-consistent calculations with different spin orientations, and N_b (with band index *n*) and N_k (with *k*-point index *k*) are the number of bands and *k* points (in first Brillouin zone), respectively. f and ϵ are the Fermi-Dirac distribution functions and the one-electron eigenvalues, respectively.

To obtain reliable values of MCA, a more precise convergence criterion of total energy was set to be 10^{-7} eV and denser $17 \times 17 \times 1$ *k*-point meshes were adopted to calculate the MCA. In the main text, Fig. 2(a) was calculated based on this method, where the positive and negative values represent the perpendicular magnetic anisotropy and in-plane anisotropy, respectively.

To gain more insight on MCA, we could evaluate the atomic and orbital-resolved contributions by projecting the SOC energy on each atom. Considering the SOC Hamiltonian $H_{\mathrm{soc}} = \frac{\hbar^2}{2m^2c^2}\frac{1}{r}\frac{dV}{dr}L \cdot S$, the matrix elements of H_{soc} in VASP can be written as [39]

$$E_{\mathrm{soc}}^{ilm,jl'm'} = \delta_{ij}\delta_{ll'} \sum_{nk} w_k f_{nk} \sum_{\alpha\beta} \langle \tilde{\psi}_{nk}^{\alpha} | \tilde{p}_{ilm} \rangle \langle \psi_{ilm}^{\alpha} | H_{\mathrm{soc}}^{\alpha\beta} | \psi_{jl'm'}^{\beta} \rangle \times \langle \tilde{p}_{jlm'} | \tilde{\psi}_{nk}^{\beta} \rangle, \tag{2}$$

where $\psi_{ilm}^{\alpha} = R_i(|r - R_i|)Y_{lm}(|r - R_i|)$ are the partial waves of an atom centered at R_i, $l(l'), m(m')$, $\alpha(\beta)$ are the angular momentum quantum number, magnetic quantum number, and the spinor component at site $R_i(R_j)$, $\tilde{\psi}_{nk}^{\alpha}$ is the spinor-component α of the pseudo-orbital with the band index n and Bloch vector k, and f_{nk} and w_k are the Fermi and k-point weights, respectively.

Since only half of the expectation value of E_{soc} can be translated into the MCA energy [40,41], the other 50% of the SOC energy is translated into the crystal-field energy and the formation of the unquenched orbital moment [40]. The atomic-resolved MCA thus can be expressed as the SOC energy difference between in-plane and out-of-plane orientation, i.e., $\mathrm{MCA}^i \approx \frac{1}{2}(E_{\mathrm{soc}}^{i,\parallel} - E_{\mathrm{soc}}^{i,\perp})$, where $E_{\mathrm{soc}}^i = \sum_{lmm'} E_{\mathrm{soc}}^{ilm,jl'm'}$ with $j = i$ and $l' = l$. The atomic-resolved MCA is used to obtain the MCA of interfacial Ru atoms in Fig. 2(b). The MCA can also be obtained by summing up the atomic-resolved MCA over all atoms, i.e., $\mathrm{MCA}_{\mathrm{tot}} = \sum_i \mathrm{MCA}^i$. Comparison of the total MCA calculated by total energy difference and by the projected SOC energies is shown in Supplemental Material Note 6 [26].

The d-orbital-resolved MCA, e.g., Figs. 2(c) and 2(d), can be extracted from VASP results using the spin-orbit matrix elements and their energy difference between in-plane and out-of-plane orientations, i.e., $\mathrm{MCA}^{ilmm'} \approx \frac{1}{2}(E_{\mathrm{soc}}^{ilm,jl'm',\parallel} - E_{\mathrm{soc}}^{ilm,jl'm',\perp})$ with $j = i$ and $l' = l$. It is noteworthy that the applied method of decomposing the MCA energy is not unique and is presumably different from other available methods [42].

The DMI strength was calculated using the chirality-dependent total energy difference approach [43] in the presence of SOC in noncollinear calculations in VASP, in which a $4 \times 1 \times 1$ $(\mathrm{SCO})_2/(\mathrm{SRO})_2$ supercell with a vacuum layer of 15 Å and a $3 \times 13 \times 1$ k mesh was adopted. Detailed information about the DMI calculations can be obtained in Supplemental Material Note 2 [26].

III. RESULTS AND DISCUSSION

A. Electronic structures

We performed DFT calculations to investigate interfacial reconstructions, as detailed in the Methods section. As depicted in Figs. 1(a) and 1(c), two ideal interfaces of the SCO/SRO heterostructures are $\mathrm{CuO_2}$-Sr-$\mathrm{RuO_2}$ and $\mathrm{CuO_2}$-SrO-$\mathrm{RuO_2}$ when the SCO and SRO is stacking along the [001] direction. For the convenience of discussion, we denote the heterostructure with the former interface as SCO/SRO-*A* and that with the latter interface as SCO/SRO-*B*. As revealed by previous experiments [44], the SRO films thicker than 2 uc is both ferromagnetic and metallic. Therefore, t_{SRO} was chosen from 2 to 6 uc in the present investigations. The SCO layer is set to 4 uc to guarantee its planar structure [45,46]. Various magnetic configurations are taken into consideration to search for magnetic ground states and the ferromagnetic state is found to be most energetically favorable in SRO layers for all heterostructures.

Our discussion in the main text will focus on the representative case of $t_{\mathrm{SRO}} = 4$ uc unless otherwise specified. For SCO/SRO-*A* [Fig. 1(a)], the surface $\mathrm{CuO_2}$ layer is buckled with the Cu ion upwards displacing with respect to the corresponding oxygen plane by $\delta_{\mathrm{Cu-O}} = 0.30$ Å, whereas the central $\mathrm{CuO_2}$ layer remains coplanar. This implies that the SCO is a polar film with a built-in electric field (Fig. S1 [26]). Meanwhile, the Sr-Sr distance is enlarged to 4.05 Å across the $\mathrm{CuO_2}$-Sr-$\mathrm{RuO_2}$ interface. This result can be attributed to electrostatic doping, similar to that observed at the $\mathrm{LaAlO_3/SrTiO_3}$ (001) interface (La-Sr distance ∼4.06 Å) [47]. However, the interfacial Ru ion only displaced vertically by $\delta_{\mathrm{Ru-O}} = -0.08$ Å, much smaller than that of the Ti ion at $\mathrm{LaAlO_3}$/ $\mathrm{SrTiO_3}$ (001) interface (∼0.17 Å) [48]. Possibly, the polar-induced effective electric field is partially screened by metallic SRO. As shown by the orbital-decomposed PDOS of Ru ions in Fig. 1(b), the spin up $d_{3z^2-r^2}$ orbital is occupied for interfacial Ru ion whereas it remains empty for the Ru ions in other SRO layers. As a consequence, the interfacial Ru ion displays a high spin state. Its projected magnetic moment is $2.10\mu_{\mathrm{B}}$/Ru while other SRO layers have a magnetic moment around 1.42 μ_{B}/Ru [Fig. 1(f)]. To get a quantitative idea about charge reconstruction, the Bader charge analysis [49] is performed. It shows that the Ru ion gains 0.33e and Cu ion loses 0.17e at the $\mathrm{CuO_2}$-Sr-$\mathrm{RuO_2}$ interface, compared to the corresponding ions in bare SRO and SCO films, respectively. Notably, the Ru ion gains more electrons than Cu ion donated. This can be ascribed to the loss of the apical oxygen of $\mathrm{RuO_6}$, leading to the formation of $\mathrm{RuO_5}$. This in turn modifies the crystal field splitting and the orbital hybridization between Ru $4d_{3z^2-r^2}$ and $5p_z$ (as shown in Fig. S2 [26]), substantially lowering the energy level of $d_{3z^2-r^2}$ orbital [50]. As a result, the nominal electron configuration of the interfacial Ru ion will be d^5 ($t_{2g}^4e_g^1$, $S = 3/2$). The projected magnetic moment is smaller than that expected for the $4d^5$-electron system (3 μ_{B}/Ru). It could be a consequence of Ru $4d$-O $2p$ hybridization. This hybridization shows its occurrence by polarizing O atom, yielding a magnetic moment of ∼ 0.24 μ_{B}/O.

For the $\mathrm{CuO_2}$-SrO-$\mathrm{RuO_2}$ interface [Fig. 1(c)], the Sr ion shifts upward by 0.42 Å with respect to the corresponding oxygen plane. This result can be attributed to the different Coulomb interaction between the $(\mathrm{CuO_2})^{2-}$ layer and the $(\mathrm{Sr})^{2+}$ or $(\mathrm{O})^{2-}$ ions. Notably, the $\mathrm{RuO_6}$ octahedron is preserved at the interface but the center Ru ion moves upward by $\delta_{\mathrm{Ru-O}} = 0.15$ Å. We also calculated the orbital-decomposed PDOS for this interface [Fig. 1(d)]. The electronic structures of four SRO layers are similar except that the spin down t_{2g} state of the interfacial Ru ion has less occupation than those in other SRO layers. This implies the occurrence of interface charge transfer, as suggested by the Bader charge analysis. We find that the Ru ion loses 0.14e and the Cu ion gains 0.08e at interface, in comparison with the bare counterparts [Fig. 1(g)]. This result confirms the charge transfer from the interfacial Ru ion to the Cu ion, with the help of the O $2p$ orbital that lifts the energy level of the spin down Ru $d_{xz/yz}$ orbital as shown

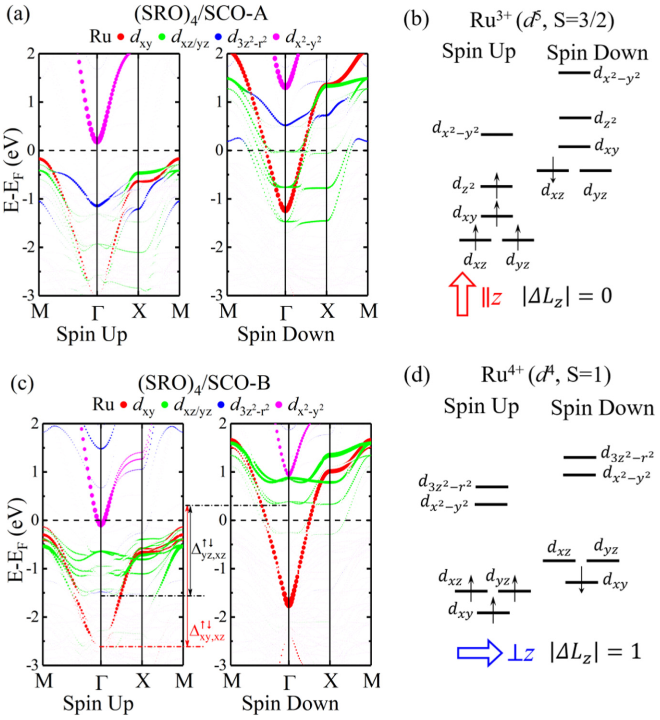

FIG. 3. Projected band structures of the interfacial Ru ion in (a) SCO/SRO-*A* and (c) SCO/SRO-*B*. The schematic electronic configurations of (b) high spin Ru^{3+} ($4d^5$, $S = 3/2$) at a square pyramidal RuO$_5$ site at the CuO$_2$-Sr-RuO$_2$ interface and (d) low spin Ru^{4+} ($4d^4$, $S = 1$) at an octahedral RuO$_6$ site at the CuO$_2$-SrO-RuO$_2$ interface. Arrow marks the magnetic easy axis.

in Fig. 3(c). In other words, the valence of the interfacial Ru ion is $+(4-\delta)$, which explains the slightly enhanced magnetic moment of the Ru ion [1.76 μ_B/Ru in Fig. 1(f)].

Following the thermodynamic approaches [51,52], the formation energy of apical oxygen vacancy located at the CuO$_2$-SrO$_{1-x}$-RuO$_2$ interface is defined as $E_f = E_A - E_B + \mu_O$, where E_A and E_B represent the DFT total energy of SCO/SRO-*A* and SCO/SRO-*B*, respectively, μ_O denotes the chemical potential of the O atom, about half the DFT energy of O$_2$. Based on this formula, we obtain the formation energy of ~2.3 eV for the apical oxygen vacancy located at the interface. This value is generally low. For example, the calculated formation energy is ~4.6 eV for bulk SRO and ~4.0 eV for the SRO/SrTiO$_3$ interface [53]. Therefore, the apical oxygen at the SCO/SRO interface is relatively easily reduced during the epitaxial growth. In other words, the CuO$_2$-Sr-RuO$_2$ interface can be easily obtained experimentally. Meanwhile, by controlling the oxygen atmosphere, the CuO$_2$-SrO-RuO$_2$ interface can also be obtained. Based on the above results, we conclude that by controlling the interfacial termination (or apical oxygen), charge and orbital reconstructions can be effectively modulated for interfacial Ru ions.

B. Magnetic anisotropy

It is an interesting topic how the interface reconstruction affects magnetic anisotropy. As is well known, the magnetic anisotropy energy (MAE) of a magnetic material generally consists of two contributions. One comes from the MCA in the electronic band structure with SOC, and the other stems from magnetic dipole interaction. We find that the contribution from magnetic dipole interaction is only ~0.04 meV/Ru [26], while the total MAE is in the order of several meV/Ru. Therefore, the MAE in our systems is mainly contributed by SOC, i.e., MAE ≈ MCA.

As shown in Fig. 2(a), the MCA oscillates with the variation of $t_{\rm SRO}$ in all systems. The positive (negative) MCA corresponds to the preferred out-of-plane (in-plane) magnetization orientation. The blue curve of MCA oscillation in Fig. 2(a) has the same trend with that of Fig. S4 in Ref. [54], which indicates that the MCA oscillation in SRO ultrathin film is universal even though calculated with different exchange functionals. Detailed discussions on this comparison can be obtained in Supplemental Material Note 7 [26]. This oscillatory behavior related with spin-polarized quantum well states has been investigated extensively in $3d$ ferromagnetic metals [55–59]. It was also reported for SRO films by Chang *et al.* [54] and was attributed to the orbital-selective quantum confinement effect of Ru t_{2g} orbitals [44]. In order to understand this oscillation, we adopt the definition of MCA based on the force theorem [38,60–62]:

$$\mathrm{MCA} \approx \int^{E_F} (E - E_F)\Delta n(E) dE, \tag{3}$$

where E_F denotes the Fermi level in collinear calculations and $\Delta n(E)$ is the difference of the density of states between different magnetization states.

For a SRO thin film on SrTiO$_3$ (001) substrate, as reported [44,63], the spin down d_{xz} and d_{yz} states form quantum well states due to the quantum confinement along the z direction, unlike the d_{xy} state that lies in the x-y plane. The biggest $\Delta n(E)$ between in-plane and out-of-plane magnetization states mainly contributed by the quantum well states located near the Fermi level [54]. In this case, even a minor tuning to $t_{\rm SRO}$ will lead to a considerable energy shift of the spin down d_{xz} and d_{yz} states, resulting in a variation of MCA in sign and magnitude. In this picture, we can understand the oscillation of MCA against $t_{\rm SRO}$ [Fig. 2(a)].

Notably, the MCA-$t_{\rm SRO}$ relation of the SCO/SRO-*A* heterostructure is similar to that of the SRO thin film but for an upward shift [Fig. 2(a)]. A similar oscillation is attributed to the similar behavior of the spin down $d_{xz/yz}$ orbital at the Fermi level in SCO/SRO-*A* heterostructure and in SRO film. As for the upward shift of the MCA-$t_{\rm SRO}$ relation, it is a consequence of the occupation of the spin up $d_{3z^2-r^2}$ orbital in the interfacial layer, which positively contributes to MCA as demonstrated by Fig. 2(c). In Fig. 2(b) we show atomic-resolved MCA for interfacial Ru ions. The MCA also displays a similar oscillation for SCO/SRO-*A* and SRO, and the MCA is always positive for SCO/SRO-*A*.

Compared to SCO/SRO-*A*, SCO/SRO-*B* displays a different MCA-$t_{\rm SRO}$ dependence. However, the MCA-$t_{\rm SRO}$ curve of SCO/SRO-*B* is nearly identical to that of SRO after a leftward shift by one uc. i.e., one SRO layer in SCO/SRO-*B* deviates from the oscillation behavior. This could be a consequence of interface reconstruction. Since spin down d_{xz} and d_{yz} orbital states of interfacial Ru ion are unoccupied [Fig. 1(d)], their difference of the density of state between different magnetization states does not contribute to the MCA based on Eq. (3). As a result, the interfacial Ru ion in SCO/SRO-*B* will not follow the similar oscillation curve with SRO films. This is consistent with the atomic-resolved MCA in Fig. 2(b), which is almost unchanged when t_{SRO} varied. As for inner SRO layers, their d_{xz} and d_{yz} orbital states are occupied and thus contribute to the MCA-t_{SRO} oscillation.

To get an idea about orbital contribution to the MCA at interface, in Figs. 2(c) and 2(d) we show the *d*-orbital-resolved MCA, which can be described by the second order perturbation theory [37,64–66]:

$$\mathrm{MCA} = \xi^2 \sum_{u,o,\sigma,\sigma'} (-1)^{1-\delta_{\sigma\sigma'}} \left[\frac{|\langle o^{\sigma'}|\hat{L}_z|u^{\sigma}\rangle|^2 - |\langle o^{\sigma'}|\hat{L}_x|u^{\sigma}\rangle|^2}{\varepsilon_u^{\sigma} - \varepsilon_o^{\sigma'}} \right], \tag{4}$$

where $u^{\sigma}(o^{\sigma'})$ and $\varepsilon_u^{\sigma}(\varepsilon_o^{\sigma'})$ stand for, respectively, the eigenstate and eigenvalue of unoccupied (occupied) orbital state d_{xy}, d_{yz}, $d_{3z^2-r^2}$, d_{xz}, or $d_{x^2-y^2}$ (here *s* and *p* orbitals have been omitted because of their negligible contributions), $\sigma(\sigma')$ represent the spin state, and δ is the kronecker function.

On the basis of Eq. (4), we are able to analyze the orbital contribution to MCA. Figure 2(c) shows the MCA for all orbital pairs for the interfacial Ru ion in the $t_{\mathrm{SRO}} = 4$ uc case of SCO/SRO-*A*. It shows that positive MCA mainly comes from the SOC term with the $\langle d_{3z^2-r^2}^{\uparrow}|L_x|d_{yz}^{\downarrow}\rangle$ matrix element, i.e., the spin-orbit coupling between occupied spin up $d_{3z^2-r^2}$ and unoccupied spin down d_{yz} orbital. In addition, $\langle d_{xz}^{\uparrow}|L_x|d_{xy}^{\downarrow}\rangle$ (or $\langle d_{xy}^{\uparrow}|L_x|d_{xz}^{\downarrow}\rangle$) also contributes a sizable positive MCA. Compared with positive MCA, negative MCA is negligibly small. For SCO/SRO-*B*, the positive MCA comes from the SOC term with the $\langle d_{xy}^{\uparrow}|L_x|d_{xz}^{\downarrow}\rangle$ matrix element. It is significantly smaller in magnitude than the negative MCA, which stems from the $\langle d_{yz}^{\uparrow}|L_z|d_{xz}^{\downarrow}\rangle$ matrix element. Since the energy difference between the occupied spin up d_{xy} and unoccupied spin down d_{xz} state, $\Delta_{xy,xz}^{\uparrow\downarrow}$, is larger than that between the occupied spin up d_{yz} and unoccupied spin down d_{xz} state, $\Delta_{yz,xz}^{\uparrow\downarrow}$, as shown in Fig. 3(c), the counteraction between the positive and negative element results in a negative MCA. Nearly identical results of the orbital-resolved MCA for the interfacial Ru ion in SCO/SRO heterostructures with different t_{SRO} are also given in Fig. S3 [26].

These results can be understood based on a simple picture of electronic configuration in terms of selection rules proposed by Whangbo *et al.* [67], in which the preferred spin orientation can be depicted using the minimum difference $|\Delta L_z|$ in the magnetic quantum numbers. The projected band structures of the Ru ions at two interfaces are shown in Figs. 3(a) and 3(c) and the corresponding electronic configurations are illustrated in Figs. 3(b) and 3(d).

As depicted in Fig. 3(b), the Ru ion at the $\mathrm{CuO_2}$-Sr-$\mathrm{RuO_2}$ interface has the electronic configuration of $(d_{xz}^{\uparrow},\ d_{yz}^{\uparrow})^2(d_{xy}^{\uparrow})^1(d_{3z^2-r^2}^{\uparrow})^1(d_{xz}^{\downarrow},\ d_{yz}^{\downarrow})^1$. Because the half-filled degenerate $(d_{xz}^{\downarrow},\ d_{yz}^{\downarrow})^1$, the highest occupied molecular orbital (HOMO), and the lowest unoccupied molecular orbit (LUMO) are degenerate with $|\Delta L_z| = 0$, the preferred spin orientation is parallel to the *z* axis. As shown in Fig. 3(d), the electronic configuration of the interfacial Ru ion at the $\mathrm{CuO_2}$-SrO-$\mathrm{RuO_2}$ interface is $(d_{xy}^{\uparrow})^1(d_{xz}^{\uparrow},\ d_{yz}^{\uparrow})^2(d_{xy}^{\downarrow})^1(d_{xz}^{\downarrow},\ d_{yz}^{\downarrow})^0$. In this case, the spin down *d* states have only the $d_{xy}^{\downarrow}$ level filled with the empty $(d_{xz}^{\downarrow},\ d_{yz}^{\downarrow})^0$ set lying immediately above. Thus, $|\Delta L_z| = 1$ occurs between HOMO and LUMO. Therefore, the preferred spin direction is perpendicular to the *z* axis, i.e, negative MCA. Obviously, the nonisostructural interface provides a promising platform for tuning magnetic anisotropy.

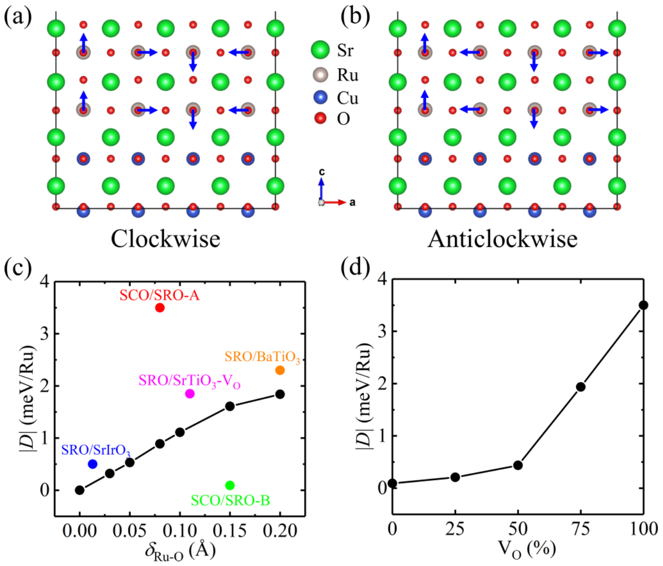

FIG. 4. (a) Clockwise and (b) anticlockwise spin configurations in SCO/SRO-*A*. (c) The DFT calculated DMI strength ($|D|$) in SCO/SRO heterostructure. For comparison, the DMI of SRO/$\mathrm{SrIrO_3}$ [68], defected-engineered SRO/$\mathrm{SrTiO_3}$ [14], SRO/$\mathrm{BaTiO_3}$ [15], and ferroelectric distorted SRO [14,15] are also plotted here as a function of $\delta_{\mathrm{Ru-O}}$, the polar shift of central Ru ion. (d) Total DMI strength $|D|$ as a function of interfacial oxygen vacancy concentration V_{O}.

C. Dzyaloshinskii-Moriya interaction

Because of the inversion symmetry breaking at interface and the sizable SOC of the Ru atom ($\xi_{\mathrm{Ru}} = 0.14\,\mathrm{meV}$ [26]), sizable interfacial DMI is expected. The constrained magnetic moment method is used to fix the direction of Ru spins as the schematic shows in Figs. 4(a) and 4(b). Given spins S_i and S_j for two neighboring Ru atoms, the DMI can be expressed by $E_{\mathrm{DMI}} = D_{ij} \cdot (S_i \times S_j)$. The DMI strength is determined using the chirality-dependent total energy difference approach [43]: $D = (E_{\mathrm{CW}} - E_{\mathrm{ACW}})/m$. Here $m = 8$ for our systems, E_{CW} and E_{ACW} represent the total energy of SCO/SRO with clockwise and anticlockwise spin configurations, respectively. The derivation of *m* is further elaborated in the Supplemental Material [26].

Figure 4(c) shows the magnitude of DMI as a function of $\delta_{\mathrm{Ru-O}}$, a vertical shift of the center Ru along the normal direction of the oxygen plane. For comparison, the reported DMI values for several typical systems and the DFT calculation-derived DMI for a bare SRO film suffering from different polar shifts ($\delta_{\mathrm{Ru-O}}$) are also included [14,15]. As shown in Fig. 4(c), the magnitude of the DMI is as large as 3.5 meV/Ru for SCO/SRO-*A* while it is only 0.1 meV/Ru for SCO/SRO-*B*:

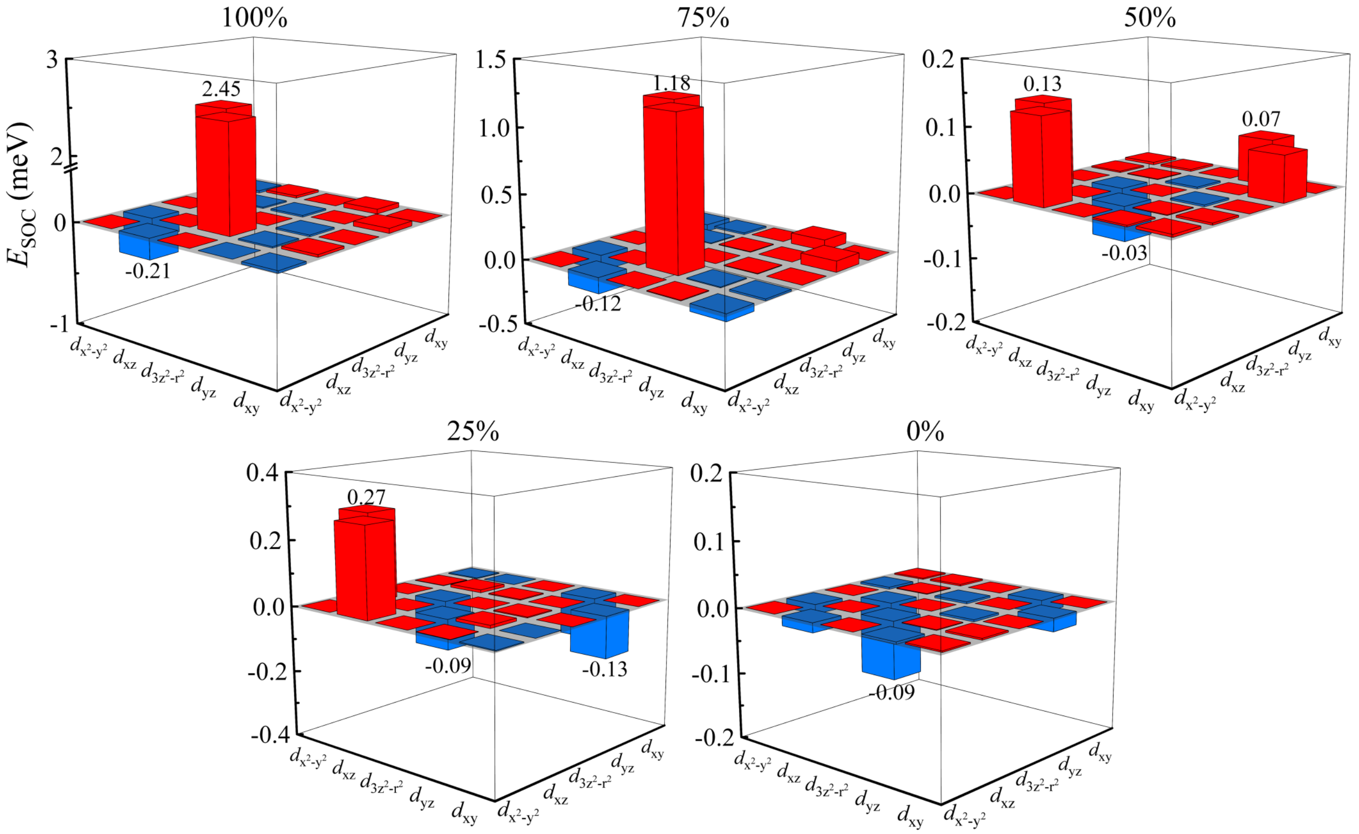

FIG. 5. Orbital-resolved contribution to DMI with different interfacial apical oxygen vacancy concentration. As the interfacial oxygen vacancy concentration varies from 100% to 0, the interfacial structure transforms from CuO_2-Sr-RuO_2 to CuO_2-SrO-RuO_2.

the DMI has been strongly modified by interfacial structure. Notably, $|D| = 3.5\,\mathrm{meV/Ru}$ is almost 1.8 times greater than the largest reported value [15]. The stability of magnetic skyrmions can be evaluated by the critical DMI $D_C = 4\sqrt{|JK|}/\pi$, where J and K are Heisenberg exchange constant and the out-of-plane magnetic anisotropy, respectively [69,70]. According to this analysis, we calculate the J between in-plane neighboring Ru ions based on the four-state method [71]. Assuming $S = 3/2$ for interfacial Ru ion, the J and D_C are calculated as -5.60 and 5.22 meV, respectively. Thus the D/J and D/D_C ratio attains 0.63 and 0.67, respectively, which is beneficial to the creation and stability of magnetic skyrmions. More than that, the DMI of SCO/SRO-*A* strongly deviates from the predicted $|D|$-$\delta_{\mathrm{Ru-O}}$ relation; it is at least three times greater than the theoretical value with the same $\delta_{\mathrm{Ru-O}}$. Obviously, the polar shift $\delta_{\mathrm{Ru-O}}$ at interface is not the main source for the DMI observed here.

To explain this deviation, we must consider interface reconstruction. As stated in Sec. III A, there exists a polar-induced electric field and an apical oxygen vacancy-induced orbital hybridization at the CuO_2-Sr-RuO_2 interface. As we smoothly decrease the content of interfacial oxygen vacancy (V_O), $|D|$ undergoes a rapid decrease [Fig. 4(d)]. Obviously, the V_O-induced orbital hybridization plays the dominative role in determining the DMI for our SCO/SRO system. To have a better understanding of the interfacial DMI, we show the orbital resolved SOC contribution to the DMI, which can be described by the first order perturbation theory [65,66]:

$$D = -mi\xi \sum_{\substack{j\neq j' \\ \sigma\neq\sigma'}} \frac{\langle \phi^{\sigma'}_{k,j'}(r)|\phi^{\sigma}_{k,j}(r)\rangle\langle\phi^{\sigma}_{k,j}(r)|L_y|\phi^{\sigma'}_{k,j'}(r)\rangle}{\varepsilon^{\sigma}_{j}-\varepsilon^{\sigma'}_{j'}}\delta_{\sigma,-\sigma'}, \tag{5}$$

where m is the exchange field, and $\phi^{\sigma}_{k,\,j}(r)$ and ε^{σ}_{j} are the eigenstate and eigenvalue of the occupied orbital state, respectively. A detailed derivation of Eq. (5) can be found in the Supplemental Material [26]. As given in Eq. (5), the DMI is directly related to the admixture of the orbital states induced by inversion symmetry breaking, i.e., the $\langle\phi^{\sigma'}_{k,j'}(r)|\phi^{\sigma}_{k,j}(r)\rangle$ term. The second term of the numerator only has three nonzero terms, i.e., $\langle d_{3z^2-r^2}|L_y|d_{xz}\rangle = \sqrt{3}$, $\langle d_{xy}|L_y|d_{yz}\rangle = 1$, and $\langle d_{x^2-y^2}|L_y|d_{xz}\rangle = 1$. The denominator $\varepsilon^{\sigma}_{j}-\varepsilon^{\sigma'}_{j'}$ is the energy difference between two different orbitals with opposite spins.

Based on Eq. (5), we are able to analyze the orbital-resolved SOC contribution to the DMI as shown in Fig. 5. When the content of apical oxygen vacancies is high, the DMI comes mainly from the positive SOC term with the $\langle d_{3z^2-r^2}|L_y|d_{xz}\rangle$ matrix element. This is understandable noting the introduction of the electron population in the $d_{3z^2-r^2}$ orbital state due to the formation of an interfacial RuO_5 square pyramid. With the introduction of oxygen ions into interface, the RuO_6 octahedron emerges, causing a decrease of the electron population in the $d_{3z^2-r^2}$ state thus a reduction of the SOC term with $\langle d_{3z^2-r^2}|L_y|d_{xz}\rangle$ matrix element. As shown in Fig. 4(d), when the interface contains 25% oxygen, the SOC term with the $\langle d_{3z^2-r^2}|L_y|d_{xz}\rangle$ matrix element is halved, and it becomes negative when 50% oxygen is introduced. Similarly, the DMI of SCO/SRO-*B* is also dominated by $\langle d_{3z^2-r^2}|L_y|d_{xz}\rangle$. In this case, the interface contains 100% oxygen, and $\langle d_{3z^2-r^2}|L_y|d_{xz}\rangle$ becomes negative.

A five tight-binding model of the Ru atom at the interface including SOC and orbital hybridization is also constructed. Further details are given in the Supplemental Material [26]. Combining the tight-binding model and Eq. (5), the DMI strength for two SCO/SRO heterostructures is obtained. The calculated DMI strengths are 3.43, 0.24 meV/Ru for the Ru ion at CuO_2-Sr-RuO_2 and CuO_2-SrO-RuO_2 interface, respectively. These results are basically identical to those obtained from the DFT calculations before. Based on these analyses, we get the conclusion that the oxygen vacancy-induced occupation of the spin up $d_{3z^2-r^2}$ orbital and orbital hybridization are pivotal for strong interfacial DMI. These results indicate that interfacing perovskite SRO with infinite-layer SCO provides a different way towards modulating interface reconstruction, leading to the effective modulation of the antisymmetric spin exchange interaction at interface, i.e., interfacial DMI.

IV. CONCLUSIONS

A theoretical investigation is presented for nonisostructural heterostructures $SrCuO_2/SrRuO_3$ with two different interfaces of CuO_2-Sr-RuO_2 and CuO_2-SrO-RuO_2. Our results show that the electronic structures, MA and DMI of the heterostructures, are strongly correlated with the interfacial structure. We present a quantitative description for atomic, charge, spin, and orbital reconstructions at interface. A high spin state of $2.1\mu_B$/Ru has been achieved at the CuO_2-Sr-RuO_2 interface, due to the depletion of apical oxygen and the polar nature of SCO. However, the interfacial Ru transforms into a low spin state of $1.7\mu_B$/Ru when the interface becomes CuO_2-SrO-RuO_2 by artificially modifying the interfacial termination. A strong oscillation of the MA with the layer thickness of SRO is observed, which gives us opportunities to tune MA. Besides, a strong DMI of 3.5 meV/Ru in the bilayers is obtained at the CuO_2-Sr-RuO_2 interface. Moreover, the DMI is tunable, monotonically decreasing with the increase of the content of the apical oxygen ions in the interfacial layer, and takes the minimal value of 0.1 meV/Ru at the CuO_2-SrO-RuO_2 interface. A quite small formation energy of apical oxygen vacancy in interfacial SRO layer is achieved, which is half as much as that in bulk SRO, indicating the experimental feasibility towards the CuO_2-Sr-RuO_2 interface. To get a deep understanding of the possible factors that influence the DMI in low-dimensional systems, we develop a tight-binding model including the spin orbit interaction and the interface symmetry breaking term. The tight-binding calculations show that the enhanced interface symmetry breaking and the occupation of $d_{3z^2-r^2}$ orbital are crucial for obtaining a sizable DMI. This work suggests that the interface design between dissimilar structures could be an effective way to realize structural modulation and provides a clear picture for the effect of interface reconstructions on MA and DMI.

ACKNOWLEDGMENTS

We thank S. Zhang for helpful discussions. This work has been supported by the Science Center of the National Science Foundation of China (Grant No. 52088101), the National Basic Research of China (Grants No. 2018YFA0305704, No. 2017YFA0303601, No. 2017YFA0206300, No. 2019YFA0704904, and No. 2016YFA0300701), the Project for Innovative Research Team of National Natural Science Foundation of China (Grant No. 11921004), the National Natural Science Foundation of China (Grants No. 11934016 and No. 51972335), and the Key Program of the Chinese Academy of Sciences. The calculations were performed in the Milky Way No. 2 supercomputer system at the National Supercomputer Center of Guangzhou, Guangzhou, China.

[1] Q. Song, H. Zhang, T. Su, W. Yuan, Y. Chen, W. Xing, J. Shi, J. Sun, and W. Han, Sci. Adv. **3**, e1602312 (2017).

[2] Y. Kozuka, S. Isogami, K. Masuda, Y. Miura, S. Das, J. Fujioka, T. Ohkubo, and S. Kasai, Phys. Rev. Lett. **126**, 236801 (2021).

[3] M. Wahler, N. Homonnay, T. Richter, A. Müller, C. Eisenschmidt, B. Fuhrmann, and G. Schmidt, Sci. Rep. **6**, 28727 (2016).

[4] Z. Qiu, Y. Kajiwara, K. Ando, Y. Fujikawa, K. Uchida, T. Tashiro, K. Harii, T. Yoshino, and E. Saitoh, Appl. Phys. Lett. **100**, 022402 (2012).

[5] S. Mühlbauer, B. Binz, F. Jonietz, C. Pfleiderer, A. Rosch, A. Neubauer, R. Georgii, and P. Böni, Science **323**, 915 (2009).

[6] B. Göbel, A. Mook, J. Henk, I. Mertig, and O. A. Tretiakov, Phys. Rev. B **99**, 060407(R) (2019).

[7] S.-H. Yang, K.-S. Ryu, and S. Parkin, Nat. Nanotechnol. **10**, 221 (2015).

[8] L. Caretta, M. Mann, F. Büttner, K. Ueda, B. Pfau, C. M. Günther, P. Hessing, A. Churikova, C. Klose, M. Schneider *et al.*, Nat. Nanotechnol. **13**, 1154 (2018).

[9] A. Soumyanarayanan, N. Reyren, A. Fert, and C. Panagopoulos, Nature (London) **539**, 509 (2016).

[10] N. Mohanta, E. Dagotto, and S. Okamoto, Phys. Rev. B **100**, 064429 (2019).

[11] D. Yi, C. L. Flint, P. P. Balakrishnan, K. Mahalingam, B. Urwin, A. Vailionis, A. T. N'Diaye, P. Shafer, E. Arenholz, Y. Choi *et al.*, Phys. Rev. Lett. **119**, 077201 (2017).

[12] Y. Gu, Y.-W. Wei, K. Xu, H. Zhang, F. Wang, F. Li, M. S. Saleem, C.-Z. Chang, J. Sun, C. Song *et al.*, J. Phys. D: Appl. Phys. **52**, 404001 (2019).

[13] E. Skoropata, J. Nichols, J. M. Ok, R. V. Chopdekar, E. S. Choi, A. Rastogi, C. Sohn, X. Gao, S. Yoon, T. Farmer *et al.*, Sci. Adv. **6**, eaaz3902 (2020).

[14] J. Lu, L. Si, Q. Zhang, C. Tian, X. Liu, C. Song, S. Dong, J. Wang, S. Cheng, L. Qu *et al.*, Adv. Mater. **33**, 2102525 (2021).

[15] L. Wang, Q. Feng, Y. Kim, R. Kim, K. H. Lee, S. D. Pollard, Y. J. Shin, H. Zhou, W. Peng, D. Lee *et al.*, Nat. Mater. **17**, 1087 (2018).

[16] J. Zhang, Z. Zhong, X. Guan, X. Shen, J. Zhang, F. Han, H. Zhang, H. Zhang, X. Yan, Q. Zhang *et al.*, Nat. Commun. **9**, 1923 (2018).

[17] H. Zhang, Y. Yun, X. Zhang, H. Zhang, Y. Ma, X. Yan, F. Wang, G. Li, R. Li, T. Khan *et al.*, Phys. Rev. Lett. **121**, 116803 (2018).

[18] D. Li, K. Lee, B. Y. Wang, M. Osada, S. Crossley, H. R. Lee, Y. Cui, Y. Hikita, and H. Y. Hwang, Nature (London) **572**, 624 (2019).

[19] Z. Liao, E. Skoropata, J. W. Freeland, E.-J. Guo, R. Desautels, X. Gao, C. Sohn, A. Rastogi, T. Z. Ward *et al.*, Nat. Commun. **10**, 589 (2019).

[20] P. E. Blöchl, Phys. Rev. B **50**, 17953 (1994).

[21] G. Kresse and J. Furthmüller, Phys. Rev. B **54**, 11169 (1996).

[22] G. Kresse and D. Joubert, Phys. Rev. B **59**, 1758 (1999).

[23] J. P. Perdew, K. Burke, and M. Ernzerhof, Phys. Rev. Lett. **77**, 3865 (1996).

[24] J. P. Perdew, A. Ruzsinszky, G. I. Csonka, O. A. Vydrov, G. E. Scuseria, L. A. Constantin, X. Zhou, and K. Burke, Phys. Rev. Lett. **100**, 136406 (2008).

[25] H. J. Monkhorst and J. D. Park, Phys. Rev. B **13**, 5188 (1976).

[26] See Supplemental Material at http://link.aps.org/supplemental/10.1103/PhysRevB.105.214428 for details about LDOS in $SrCuO_2$ region, interfacial Ru $4d3z2$-$r2$-$5pz$ hybridization, the orbital-resolved MCA in SCO/SRO systems with different t_{SRO}, the tests for MCA in calculations, the MAE contributed from magnetic dipole interaction, the comparison of total MCA obtained from two different methods, the DMI derivation, and the tight-binding calculations, which includes Refs. [72–76].

[27] K. Gupta, B. Mandal, and P. Mahadevan, Phys. Rev. B **90**, 125109 (2014).

[28] S. L. Dudarev, G. A. Botton, S. Y. Savrasov, C. J. Humphreys, and A. P. Sutton, Phys. Rev. B **57**, 1505 (1998).

[29] V. I. Anisimov, J. Zaanen, and O. K. Andersen, Phys. Rev. B **44**, 943 (1991).

[30] B. Geisler and R. Pentcheva, Phys. Rev. Research **3**, 013261 (2021).

[31] Y. Zhang, L.-F. Lin, W. Hu, A. Moreo, S. Dong, and E. Dagotto, Phys. Rev. B **102**, 195117 (2020).

[32] J. Neugebauer and M. Scheffler, Phys. Rev. B **46**, 16067 (1992).

[33] S. H. Chang, Y. J. Chang, S. Y. Jang, D. W. Jeong, C. U. Jung, Y.-J. Kim, J.-S. Chung, and T. W. Noh, Phys. Rev. B **84**, 104101 (2011).

[34] D. Hobbs, G. Kresse, and J. Hafner, Phys. Rev. B **62**, 11556 (2000).

[35] M. Marsman and J. Hafner, Phys. Rev. B **66**, 224409 (2002).

[36] M. Blanco-Rey, J. I. Cerda, and A. Arnau, New J. Phys. **21**, 073054 (2019).

[37] G. H. O. Daalderop, P. J. Kelly, and M. F. H. Schuurmans, Phys. Rev. B **41**, 11919 (1990).

[38] M. Weinert, R. E. Watson, and J. W. Davenport, Phys. Rev. B **32**, 2115 (1985).

[39] S. Steiner, S. Khmelevskyi, M. Marsmann, and G. Kresse, Phys. Rev. B **93**, 224425 (2016).

[40] R. Skomski, A. Kashyap, and A. Enders, J. Appl. Phys. **109**, 07E143 (2011).

[41] V. Antropov, L. Ke, and D. Aberg, Solid State Commun. **194**, 35 (2014).

[42] M. Cinal, Phys. Rev. B **105**, 104403 (2022).

[43] H. Yang, A. Thiaville, S. Rohart, A. Fert, and M. Chshiev, Phys. Rev. Lett. **115**, 267210 (2015).

[44] Y. J. Chang, C. H. Kim, S.-H. Phark, Y. S. Kim, J. Yu, and T. W. Noh, Phys. Rev. Lett. **103**, 057201 (2009).

[45] Z. Zhong, G. Koster, and P. J. Kelly, Phys. Rev. B **85**, 121411(R) (2012).

[46] D. Samal, H. Tan, H. Molegraaf, B. Kuiper, W. Siemons, S. Bals, J. Verbeeck, G. Van Tendeloo, Y. Takamura, E. Arenholz *et al.*, Phys. Rev. Lett. **111**, 096102 (2013).

[47] B. Geisler, A. Blanco-Romero, and R. Pentcheva, Phys. Rev. B **95**, 125301 (2017).

[48] R. Pentcheva and W. E. Pickett, Phys. Rev. B **78**, 205106 (2008).

[49] W. Tang, E. Sanville, and G. Henkelman, J. Phys.: Condens. Matter **21**, 084204 (2009).

[50] C. Lin and A. A. Demkov, Phys. Rev. Lett. **111**, 217601 (2013).

[51] G.-X. Qian, R. M. Martin, and D. J. Chadi, Phys. Rev. B **38**, 7649 (1988).

[52] C. G. Van de Walle, D. B. Laks, G. F. Neumark, and S. T. Pantelides, Phys. Rev. B **47**, 9425 (1993).

[53] J. Lu, L. Si, X. Yao, C. Tian, J. Wang, Q. Zhang, Z. Lai, I. A. Malik, X. Liu, P. Jiang *et al.*, Phys. Rev. B **101**, 214401 (2020).

[54] A. Huang, H.-T. Jeng, and C.-H. Chang, ACS Appl. Nano Mater. **4**, 5932 (2021).

[55] W. Weber, A. Bischof, R. Allenspach, C. Würsch, C. H. Back, and D. Pescia, Phys. Rev. Lett. **76**, 3424 (1996).

[56] M. Cinal and D. M. Edwards, Phys. Rev. B **57**, 100 (1998).

[57] G. Y. Guo, J. Phys.: Condens. Matter **11**, 4329 (1999).

[58] M. Cinal, J. Phys.: Condens. Matter **15**, 29 (2003).

[59] L. M. Sandratskii, Phys. Rev. B **92**, 134414 (2015).

[60] D. Li, A. Smogunov, C. Barreteau, F. Ducastelle, and D. Spanjaard, Phys. Rev. B **88**, 214413 (2013).

[61] X. Wang, D.-S. Wang, R. Wu, and A. J. Freeman, J. Magn. Magn. Mater. **159**, 337 (1996).

[62] G. H. O. Daalderop, P. J. Kelly, and M. F. H. Schuurmans, Phys. Rev. B **50**, 9989 (1994).

[63] S. Kang, Y. Tseng, B. H. Kim, S. Yun, B. Sohn, B. Kim, D. McNally, E. Paris, C. H. Kim, C. Kim *et al.*, Phys. Rev. B **99**, 045113 (2019).

[64] X. Chen, S. Zhang, B. Liu, F. Hu, B. Shen, and J. Sun, Phys. Rev. B **100**, 144413 (2019).

[65] X. Wang, R. Wu, D.-S. Wang, and A. J. Freeman, Phys. Rev. B **54**, 61 (1996).

[66] D. S. Wang, R. Wu, and A. J. Freeman, Phys. Rev. B **47**, 14932 (1993).

[67] M.-H. Whangbo, E. E. Gordon, H. Xiang, H.-J. Koo, and C. Lee, Acc. Chem. Res. **48**, 3080 (2015).

[68] J. Matsuno, N. Ogawa, K. Yasuda, F. Kagawa, W. Koshibae, N. Nagaosa, Y. Tokura, and M. Kawasaki, Sci. Adv. **2**, e1600304 (2016).

[69] A. Bogdanov and A. Hubert, J. Magn. Magn. Mater. **138**, 255 (1994).

[70] A. Fert, N. Reyren, and V. Cros, Nat. Rev. Mater. **2**, 17031 (2017).

[71] H. J. Xiang, E. J. Kan, S.-H. Wei, M.-H. Whangbo, and X. G. Gong, Phys. Rev. B **84**, 224429 (2011).

[72] L. M. Sandratskii, J. Phys.: Condens. Matter **3**, 8565 (1991).
[73] M. Heide, G. Bihlmayer, and S. Blügel, Phys. B: Condens. Matter **404**, 2678 (2009).
[74] A. A. Mosstofi, J. R. Yates, G. Pizzi, Y.-S. Lee, I. Souza, D. Vanderbilt, and N. Marzari, Comput. Phys. Commun. **185**, 2309 (2014).
[75] G. Pizzi, V. Vitale, R. Arita, S. Blügel, F. Freimuth, G. Géranton, M. Gibertini, D. Gresch, C. Johnson, T. Koretsune *et al.*, J. Phys.: Condens. Matter **32**, 165902 (2020).
[76] K. V. Shanavas, Z. S. Popović, and S. Satpathy, Phys. Rev. B **90**, 165108 (2014).